Dalton Transactions

RSC Publishing

COMMUNICATION

View Article Online
View Journal | View Issue

Cite this: *Dalton Trans.*, 2013, **42**, 15931

Received 26th June 2013,
Accepted 28th August 2013

DOI: 10.1039/c3dt51703a

www.rsc.org/dalton

Bottom-up assembly of ultrathin sub-micron size metal–organic framework sheets†

Rie Makiura*[a,b,c] and Oleg Konovalov[d]

A solution-based two-dimensional interfacial reaction between 5,10,15,20-tetra(4-pyridyl)-porphinato zinc(II) (ZnTPyP, 1) and $Cu(NO_3)_2{\cdot}3H_2O$, 2, results in the assembly of uniform preferentially oriented highly crystalline metal–organic framework nanosheets, NAFS-21 that have sub-micron planar size and mono-molecular thickness.

Coordination materials including porous compounds called porous coordination polymers (PCP) or metal–organic frameworks (MOFs) have been in the spotlight of organic–inorganic hybrid solid research for the rich variety of both framework and nanopore design arising from the virtually unlimited combinations of metal ions and organic molecular building components, while providing a number of potential applications ranging from a high amount of gas storage to drug delivery.[1] However, controlling the dimensionality and size of the materials at the nanoscale and aligning them on/with various substances in desired ways have remained a challenge although reports on controlling their size and shape have been increasing in recent years.[2]

Two-dimensional (2D) sheets with monomolecular thickness have been attracting considerable attention as they can be envisaged as prototype materials for ultrathin, transparent and flexible nanodevices with novel functionality features derived from their intrinsic 2D properties.[3–8] Two approaches have been mainly attempted in preparing such 2D nanosheets: top-down exfoliation from the bulk crystals and bottom-up assembly of atomic/molecular building units *via* a variety of structure-directing interactions including covalent, coordination, hydrogen and van der Waals bonding. Many kinds of 2D nanosheets have been prepared by the top-down exfoliation process including graphene,[4] metal oxides,[5] transition-metal chalcogenides[6] and organic polymers.[7] On the other hand, an ultimate goal in the field is to prepare them by the bottom-up approach utilizing the self-assembling features of the building units and to align them on various substrates. The creation of 2D sheet assemblies of PCPs or MOFs and their layering in any desired way will bring a brighter future not only for the nanotechnological thin film devices but also for nanofilters such as multifunctional membranes possessing separation, reaction and condensation functionalities.

We have succeeded recently in creating crystalline and perfectly-oriented MOF thin films with nanometer scale thickness (NAFS-1, NAFS-2; nanofilm of metal–organic frameworks on surfaces no. 1 and no. 2) prepared by a facile solution-based method at ambient temperature.[9,10] NAFS films have layered structures – 2D molecular networks are formed at the air–liquid interface by metal-directed self-assembly of appropriate building units, then transferred to a solid surface, and finally stacked following a layer-by-layer (LbL) protocol. The 2D molecular assemblies are created by a modified Langmuir–Blodgett (LB) film fabrication technique. The highly-crystalline order of the coordinative NAFS architecture was directly proven by synchrotron X-ray crystallography. Both NAFS-1 and NAFS-2 are composed of porphyrin derivatives containing four peripheral carboxylic groups – each porphyrin molecular unit is connected *via* copper ion linkers, which form paddle-wheel dimeric $Cu_2(COO)_4$ secondary building units, thereby resulting in the creation of a nanosheet with a checkerboard grid structure.[9,10] Thus far such highly crystalline mono-molecular MOF nanosheets have been achieved only with porphyrin-based molecular building units containing carboxylic acid groups. In order to utilize such ultrathin MOF nanosheets in various applications, modification of the building unit and structure (including pore size and shape), which influence sheet characteristics such as electronic properties and ion/molecular trapping/transfer, is necessary. Furthermore, enlargement of the nanosheet size is an additional important issue to be addressed[11] – for instance, the sheets should be large enough

[a]*Nanoscience and Nanotechnology Research Center, Research Organization for the 21st Century, Osaka Prefecture University, Sakai, Osaka 599-8570, Japan. E-mail: r-makiura@21c.osakafu-u.ac.jp; Fax: +81 72 254 985; Tel: +81 72 254 985*
[b]*PRESTO, Japan Science and Technology Agency, Saitama, Japan*
[c]*CREST, Japan Science and Technology Agency, Saitama, Japan*
[d]*European Synchrotron Radiation Facility, Grenoble Cedex 38043, France*

†Electronic supplementary information (ESI) available: π-A isotherms, UV-Vis absorption spectra, GIXRD and XRR of the ZnTPyP arrays on the pure water subphase. See DOI: 10.1039/c3dt51703a

to connect patterned electrodes or to minimize the influence of defects at the sheet edges when we consider them for use in electronic devices. The crystalline domain size of the NAFS nanosheets is estimated at about 140 nm for sheets composed of $Cu_2(COO)_4$ building units formed at the air–liquid interface – *in situ* synchrotron X-ray diffraction has revealed that the sheet size is determined by the initial interfacial reaction between molecular building units and metal ion linkers.[10b] One of the ways to tune the metal–ligand interfacial coordinative reaction is to vary the coordinative ligands. Instead of using carboxylic acid groups whose protons are removed and negatively charged carboxylate units connect to the metal ions, here we employed neutral pyridyl groups as the peripheral porphyrin substituents, in an attempt to slow down the interfacial reaction that leads to the formation of the metal–ligand coordinative bonds. At the same time, we expect that the lattice size becomes smaller than that in NAFS-1 and NAFS-2 as now the peripheral pyridyl units are smaller than the phenyl carboxylate ones.

The fabrication protocol was initiated by spreading a solution of the tetratopic molecular building unit, 5,10,15,20-tetra(4-pyridyl)-porphinato zinc(II) (ZnTPyP, **1**), onto an aqueous solution of $Cu(NO_3)_2{\cdot}3H_2O$, **2**, at room temperature in a Langmuir trough. In order to follow the formation of the ordered arrays composed of ZnTPyP molecules and copper ions (ZnTPyP-Cu, NAFS-21) on the surface, the surface pressure (π) was monitored using a Wilhelmy plate during surface compression by a movable barrier (Fig. 1) and the mean molecular areas of the arrays and the number of ZnTPyP molecules spread were evaluated. The same ZnTPyP spread solution was applied onto a pure water subphase for comparison. In the case of the copper ion aqueous solution subphase, the mean molecular area of ~190 Å^2 observed at a surface pressure of around 5–10 mN m^{-1} (Fig. S1†) is in excellent agreement with the value of 188 Å^2 calculated considering the NAFS-21 nanosheet molecular arrangement in which the ZnTPyP molecules lie flat on the surface and are connected *via* coordinative bonds between the four peripheral pyridyl substituents of ZnTPyP and copper ions (*vide infra*). This is also consistent with the larger molecular area observed for the NAFS-21 nanosheet in the surface pressure–molecular area (π–*A*) isotherms (Fig. S1†). On the other hand, when pure water is used as the subphase, the smaller mean molecular area observed implies that the ZnTPyP molecules now pack more closely. The molecular arrangements derived by the π–*A* isotherms are supported by UV-vis absorption spectroscopy measurements of nanosheets transferred onto quartz substrates (Fig. S2†). The change in the shape of the Soret band of ZnTPyP in the NAFS-21 nanofilm indicates that a change of the electronic state of ZnTPyP is induced through the coordination between the peripheral pyridyl parts of ZnTPyP and the copper ions.[12] In addition, the smaller absorbance observed for the NAFS-21 nanosheets implies that fewer ZnTPyP molecules exist in the same area of the sheet than in the array formed on the pure water subphase. This again supports the proposed molecular arrangement in NAFS-21 derived from the π–*A* isotherm measurements (Fig. S1†). Infrared (IR) absorption spectra measurements also confirm that no exchange reaction between central Zn^{2+} ions of ZnTPyP and Cu^{2+} ions in the substrate solution occurs in the course of the formation process of the NAFS-21 nanofilms at the air–liquid interface (Fig. S3†).

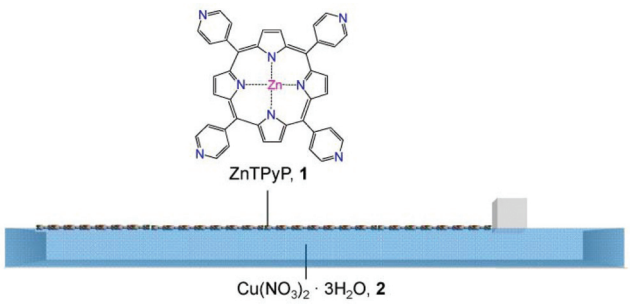

Fig. 1 Schematic illustration of the assembly process of the ZnTPyP-Cu metal–organic framework nanosheets (NAFS-21) at the air–liquid interface. The solution of ZnTPyP molecular building units, **1**, is spread onto the $Cu(NO_3)_2{\cdot}3H_2O$ aqueous solution, **2**, in a Langmuir trough. The surface pressure, π, is controlled by the movement of a single one-side barrier.

The evolution of the sheet morphology and surface coverage of the NAFS-21 nanosheets at the air–liquid interface during compression was followed by Brewster angle microscopy (BAM). BAM images at various surface pressure points are shown in Fig. 2 together with the π–*A* isotherm of NAFS-21. A featureless image was observed in the absence of spread molecules on the surface (Fig. 2a). After spreading the ZnTPyP solution onto the copper ion subphase and before surface compression (π = 0 mN m^{-1}), a number of randomly floating sheet domains were observed (Fig. 2b). The image was captured during the sheet movement. After initiating surface compression, floating sheets were still observed even without barrier movement until the surface pressure, π, reached about 5 mN m^{-1} when their motion slowed down (Fig. 2c and 2d; π = 1 and 5 mN m^{-1}, respectively). When π increased up to about 10 mN m^{-1}, the sheet movement stopped completely (Fig. 2e, π = 12 mN m^{-1}), implying that all sheets were now connected forming a continuous film on the surface of the trough. Only when the barrier moved again and the surface pressure increased was any further shift in the sheet domains observed (Fig. 2f, π = 25 mN m^{-1}). Black parts indicating a liquid surface without any sheet coverage still remain up to π = 25 mN m^{-1}. When the surface pressure reached 35 mN m^{-1}, a white line clearly appeared, implying that the edges of neighbouring sheets were now touching and squeezing against each other, resulting in the creation of bumps (Fig. 2g, π = 35 mN m^{-1}). Further compression caused cracks in the sheets that appeared in the images as black lines (Fig. 2h, π = 40 mN m^{-1}).

Detailed structural information, including the molecular arrangement of NAFS-21 formed at the air–liquid interface, was obtained by *in situ* synchrotron X-ray diffraction (XRD, λ = 1.549 Å) measurements with a dedicated PTFE trough installed in the diffractometer at the ESRF beamline, ID10B.[13] The XRD measurements were carried out directly at the air–liquid

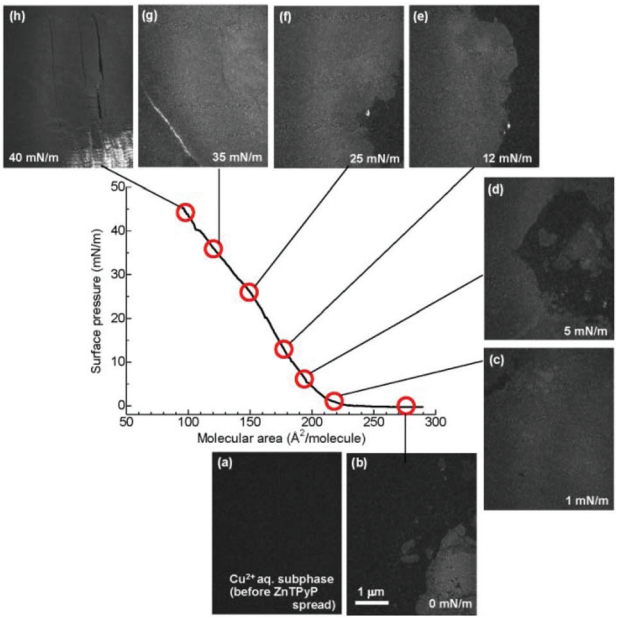

Fig. 2 Brewster angle microscopy (BAM) images of the NAFS-21 nanosheets at the air–water interface captured during compression. (a) Surface of the Cu^{2+} ion aqueous solution subphase before spreading ZnTPyP molecules, (b) at 0 mN m^{-1}, after spreading ZnTPyP molecules, (c) at 1 mN m^{-1}, (d) at 5 mN m^{-1}, (e) at 12 mN m^{-1}, (f) at 25 mN m^{-1}, (g) at 35 mN m^{-1} and (h) at 40 mN m^{-1}. Before surface compression, a number of randomly moving domains were observed – the image was captured while the domains floated through the monitor. Black parts represent exposed liquid surface. After surface compression was initiated, the movement of the domains slowed down. Large sheet domains were observed even at low surface pressures, $\pi \sim 1$ mN m^{-1}. As the surface pressure started increasing, the density of black parts became smaller and no black parts were observed at 35 mN m^{-1}. However, a white line clearly appeared at 35 mN m^{-1}, implying that neighbouring sheet edges were now touching, leading to the creation of bumps. Further compression caused cracks in the sheets which appeared as black lines.

interface in grazing incidence (GI) in-plane mode with the incident angle of 0.12° to the liquid surface, as illustrated in the inset of Fig. 3a. Fig. 3a shows the observed in-plane XRD pattern for the NAFS-21 sheet collected at a surface pressure, π = 5 mN m^{-1}, together with the simulated profile for the structural model shown in Fig. 3b. Four sharp diffraction peaks are observed up to a scattering angle, $2\theta_{xy}$, of 19° and the index as (110), (200), (210) and (220) on a metrically tetragonal unit cell with basal plane dimensions, $a = b$ = 13.710(8) Å. Importantly, all Bragg reflections observed with the GI in-plane geometry can be indexed as (hk0) and the observed in-plane XRD profile is in excellent agreement with the simulated pattern. This not only proves that NAFS-21 is characterized by highly crystalline order in the in-plane direction with a 2D "checkerboard" molecular assembly of ZnTPyP molecular units directed by copper ions as shown in Fig. 3b, but also signifies that the NAFS-21 sheets are perfectly preferentially oriented – the sheet plane is parallel to the liquid surface.

Further information about the sheet organization and orientation of the NAFS-21 nanosheets was obtained using 2D GIXRD patterns. Fig. 4a shows the reciprocal space map of the diffracted intensity for each reflection (scattering rod) along scattering angles horizontal, $2\theta_{xy}$, and vertical, $2\theta_z$, to the interface, collected at the air–liquid interface at a surface pressure, π = 5 mN m^{-1}. All scattering rods are parallel to the vertical scattering angle, $2\theta_z$, axis, unambiguously proving that the NAFS-21 nanosheets are perfectly oriented with the 2D sheet plane aligned strictly parallel to the liquid surface. A GI in-plane XRD profile of NAFS-21 obtained from integration of the 2D image in the range, $2\theta_z$ = 0–0.5°, is shown in Fig. 4b. The inset shows the selected region around the most intense (110) Bragg reflection (black dots) whose full width at half maximum (FWHM) is evaluated to be 0.0801(6)° – this is identical to the instrumental resolution (0.08°) of the experimental setup and implies that the diffraction peak widths of the

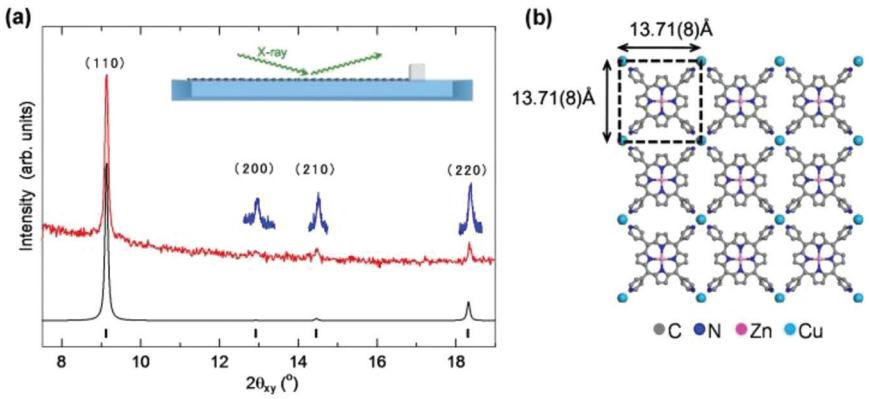

Fig. 3 (a) *In situ* grazing incidence in-plane synchrotron X-ray diffraction (GIXRD) pattern (red line, λ = 1.549 Å, incidence angle, α = 0.12°) collected at the air–liquid interface for NAFS-21 nanosheets at a surface pressure, π = 5 mN m^{-1}. The blue lines are higher statistics fine scans collected in the vicinity of the three weaker diffraction peaks. All four observed peaks up to a scattering angle, 2θ = 19°, index as (hk0) on a metrically tetragonal unit cell with basal plane dimensions, $a = b$ = 13.71(8) Å (the Miller indices of the Bragg peaks are (110), (200), (210) and (220) in the order of increasing scattering angle). The calculated in-plane XRD profile (black line) for the structural model depicted in (b) is also shown with the positions of the Bragg reflections shown as black tick marks. (b) Basal plane projection of the crystalline structure of NAFS-21, which consists of a 2D "checkerboard" motif of ZnTPyP units linked by copper ions. The black dashed lines mark the in-plane square unit cell. C atoms are shown in grey, N atoms in blue, Zn^{2+} ions in pink, and Cu^{2+} ions in pale blue colour.

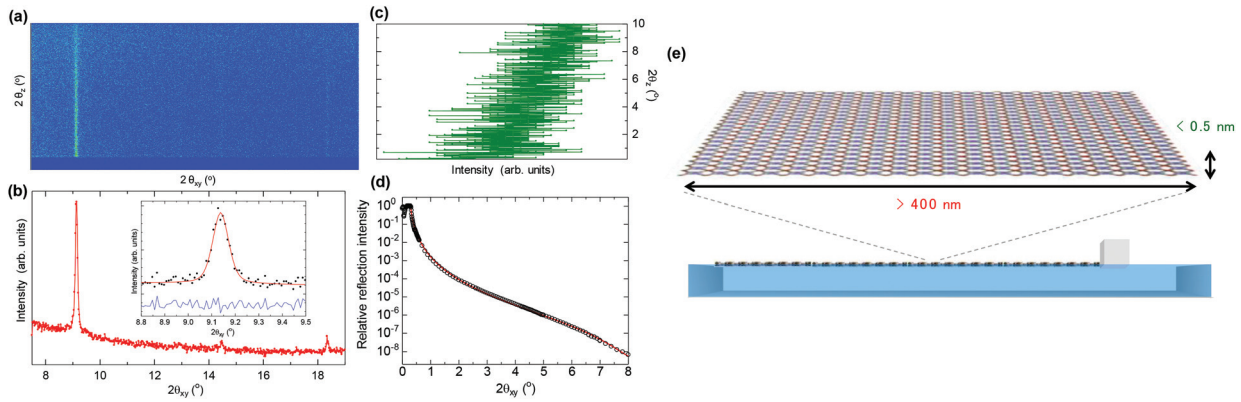

Fig. 4 (a) *In situ* grazing incidence X-ray diffraction reciprocal space map (diffracted intensity along $2\theta_{xy}$ (horizontal) and $2\theta_z$ (vertical) diffraction angles, λ = 1.549 Å, incidence angle, α = 0.12°) of the NAFS-21 nanosheets collected at the air–liquid interface at a surface pressure, π = 5 mN m^{-1}. (b) Integrated in-plane XRD profile (summed over the vertical diffraction angle, $2\theta_z$ range of 0–0.5°). The *inset* shows observed (solid circles) and fitted (red solid line) profiles in the vicinity of the (110) Bragg reflection. The lower blue solid line shows the difference profile. (c) Out-of-plane XRD profile obtained following integration of the XRD 2D map over the $2\theta_{xy}$ range of 9.08–9.17° in the vicinity of the (110) Bragg reflection. (d) Observed (black circle) and fitted (two-layer model, red solid line) *in situ* X-ray reflectivity profile of the NAFS-21 nanosheets collected at the air–liquid interface at a surface pressure, π = 1 mN m^{-1}. (e) Schematic illustration of the high aspect ratio NAFS-21 nanosheets (width >400 nm, thickness <0.5 nm) assembled at the air–liquid interface.

NAFS-21 nanosheets are resolution limited. We can thus extract a lower limit of the average crystalline domain size of the nanosheets – their coherence length in the direction parallel to the 2D sheet plane – as 410 nm from the resolution limited fitted FWHM using Scherrer's equation. Even this lower bound of the sheet domain size is three times larger than that of the nanosheets composed of porphyrin molecules with phenylcarboxylate peripheral groups.[10]

Next, the NAFS-21 sheet thickness – the coherence length along the surface normal – was evaluated by examining the integrated out-of-plane line profiles of the Bragg reflections as a function of the vertical scattering angle, $2\theta_z$. The out-of-plane profile of the (110) reflection integrated in the range $2\theta_{xy}$ = 9.08–9.17° (Fig. 4c) shows a gradual decrease in intensity with increasing scattering angle in the range $2\theta_z$ = 0–10°. This leads to an estimated lower limit of the FWHM of the out-of-plane profile of 3°, which in turn defines an upper bound for the sheet thickness of 0.5 nm, which corresponds to the single-molecule sheet thickness.

Complementary information about the thickness and morphology of the NAFS-21 nanosheets was derived from the *in situ* X-ray reflectivity (XRR) measurements at the air–liquid interface (Fig. 4d). The observed XRR curve (black circles) is fitted well with a two-layer model (red solid line), one for the water substrate layer and one for the NAFS-21 monolayer. The variable parameters of the model included the film thickness and the density of the NAFS-21 nanosheet – these were deduced as 0.497(2) nm and 0.577(3) g cm^{-3}, respectively, after fixing the density of the water substrate to 1.0 g cm^{-3}. The derived film thickness from the XRR curve fitting is in excellent agreement with that estimated from the FWHM of the out-of-plane XRD profile. Moreover, allowing the film roughness to vary led to a value of 0 nm, demonstrating that the NAFS-21 sheet surface is also remarkably smooth.

We also performed comparable XRD and XRR measurements for ZnTPyP arrays spread on a pure water subphase – the 2D GIXRD image and the XRR curve are shown in Fig. S4 and S5,† respectively. The striking difference between the present 2D image and that of NAFS-21 formed on the copper ion aqueous solution (Fig. 4a) and the absence of rod scattering in the image of the ZnTPyP array on the pure water surface (Fig. S4a†) confirm that highly oriented molecular sheets form only in the presence of copper ions in the subphase. The film thickness and the density of the ZnTPyP array on the pure water subphase were evaluated as 0.91(3) nm and 1.041(7) g cm^{-3}, respectively – both values are significantly larger than those of NAFS-21 (0.497(2) nm and 0.577(3) g cm^{-3}, respectively), implying that the ZnTPyP arrays without copper ions present form densely packed sheets in which the ZnTPyP molecules stand on the water surface at some angle. The appearance of a broad diffuse scattering hump whose peak is around $2\theta_{xy}$ = 25° (d spacing ≈ 3.6 Å) in the integrated in-plane XRD profile (summed over the vertical diffraction angle, $2\theta_z$ range of 0–0.5°) (Fig. S4b†) also supports this molecular arrangement on the pure water subphase. In addition, the surface roughness for ZnTPyP on pure water is estimated as 0.419(7) nm, while that of the NAFS-21 nanosheets is ~0 nm, implying that the interfacial reaction of the ZnTPyP molecules and the copper ions resulted in the creation of ultrathin nanosheets that were not only highly crystalline and preferentially oriented but also uniform and smooth. A schematic illustration of the ultrathin NAFS-21 nanosheets assembled on the air–liquid interface derived from the *in situ* suite of synchrotron X-ray experiments is shown in Fig. 4e – sizeable (lower bound of lateral sheet size ~410 nm), ultrathin (upper bound of vertical sheet size ~0.5 nm), perfectly preferentially-oriented morphologically-uniform MOF nanosheets were successfully formed. The lateral-to-vertical aspect ratio of the NAFS-21

sheets exceeds 820 with each sheet containing in excess of 90 000 ZnTPyP molecules.

In summary, we have successfully created smooth ultrathin metal–organic framework nanosheets, NAFS-21, whose sheet size approaches sub-micron dimensions by a bottom-up approach utilizing the air–liquid interface under ambient conditions. The NAFS-21 nanosheets are assembled by the interfacial reaction between tetratopic porphyrin-based molecular building units with pyridyl coordinative groups and structure-directing copper ion joints. *In situ* GIXRD measurements at the interface reveal that the NAFS-21 sheets are of mono-molecular thickness (less than 0.5 nm tall) with a crystalline domain size in the direction parallel to the liquid surface of sub-micron scale, larger than 410 nm – as the XRD peak widths were limited by the resolution of the present synchrotron X-ray diffraction experimental setup, the precise sheet size is expected to be larger, approaching the μm scale. We will investigate further the integrity and structural characteristics of NAFS-21 and related nanosheets with a higher resolution synchrotron XRD setup that will allow us to probe *in situ* the growth of 2D sheets with domain sizes as large as 4–5 μm in the future.

Experimental section

5,10,15,20-Tetra(4-pyridyl)-porphinato zinc(II) (ZnTPyP, **1**) and $Cu(NO_3)_2{\cdot}3H_2O$ (>99.9%, **2**) were purchased from Sigma-Aldrich Co. Pure grades of chloroform and methanol were purchased from Waco Pure Chemical Industries Ltd or Sigma-Aldrich Co. All chemicals were used as received without further treatment.

A PTFE-coated Langmuir trough (460 × 170 × 5 mm^3) was filled with an aqueous solution of $Cu(NO_3)_2{\cdot}3H_2O$, **2** (10 mM) as a subphase. The surface of the subphase was carefully cleaned by mild surface-touch vacuuming. 190 μL of a 0.2 mM solution of ZnTPyP, **1**, in mixed chloroform–methanol solvent (3 : 1, v/v) was spread onto the $Cu(NO_3)_2$ subphase with a microsyringe. Surface pressure–area (π–A) isotherm measurements were performed at a continuous pressing speed for the barrier of 500 μm s^{-1} at room temperature. The surface pressure was measured by the Wilhelmy plate method. 350 μL of the same 0.2 mM ZnTPyP solution was also spread onto a pure water subphase and π–A isotherms were measured for comparison.

The formation and morphology of the sheets in the Langmuir trough were followed by BAM experiments performed with a NIMA Technology BAM model 712 system in which a PTFE Langmuir trough (750 × 100 mm^2) with two compression barriers was installed. The ZnTPyP films were prepared as described above. The laser wavelength was 532 nm. The incidence angle of the laser light was adjusted to 53.12° (the magnitude of the Brewster angle for the air–water interface) with respect to the surface normal. Images of the films at the air–liquid interface were captured by a CCD camera at room temperature.

In situ synchrotron GIXRD and XRR measurements were performed at room temperature using the six-circle diffractometer on beamline ID10B (E = 8.003 keV, λ = 1.549 Å) at the ESRF (Grenoble, France). The dedicated PTFE Langmuir trough (460 × 170 × 5 mm^3) mounted on the diffractometer was equipped with a single movable barrier for the film compression. The ZnTPyP sheets were prepared as described above. The surface pressure was kept constant during individual GIXRD and XRR measurements. The Langmuir trough was mounted on an active antivibration system and was enclosed inside an air-tight acrylic case with polyimide windows. Water-saturated helium gas was introduced into the case. The incidence angle for the GIXRD measurements was set as 0.12°. The scattered X-rays were recorded by a one-dimensional (1D) gas-filled position-sensitive detector with vertically located counting wires (VANTEC). The XRD profiles were collected by scanning over the in-plane θ angle and the vertical (out-of-plane) scattered intensity was recorded at each 2θ angle. In order to improve the 2θ resolution to the in-plane direction and reduce background contribution, a Soller collimator (0.08°) was placed in front of the 1D detector. XRR data were collected using a two-dimensional (2D) gas-filled position-sensitive detector at the glancing angular range by a θ–2θ scan in the out-of-plane geometry. The average sheet domain size was estimated with Scherrer's equation using a value for the Scherrer's constant of 1.84, appropriate for (*hk*) Bragg reflections of layer-structured crystalline materials.

UV-vis absorption spectra of the ZnTPyP-based sheets deposited on quartz glass substrates were measured using a Jasco V-670 spectrophotometer at room temperature. IR spectra of NAFS-21 nanosheets deposited on a Si substrate and of reference bulk materials were measured using a Jasco FT/IR-6200 system at room temperature.

We thank the Japan Society for the Promotion of Science (JSPS) "Grants-in-Aid for Scientific Research on Innovative Areas for Coordination Programming (22108524, 24108735)", the Japan Science and Technology Agency (JST) "Precursory Research for Embryonic Science and Technology (PRESTO)" for a project titled "Molecular technology and creation of new functions", "the Core Research for Evolutional Science and Technology (CREST)", the Ministry of Education, Culture, Sports, Science and Technology (MEXT) "Special Coordination Funds for Promoting Science and Technology (SCF)", the Kao Foundation for Arts and Sciences, the INAMORI foundation, the Japan Prize Foundation and the Royal Society (UK) "International Exchange Scheme" for financial support, and the European Synchrotron Radiation Facility (ESRF), Grenoble, France for access to the synchrotron X-ray facilities and the use of the BAM instrumentation.

Notes and references

1 (*a*) S. Kitagawa, R. Kitaura and S. Noro, *Angew. Chem., Int. Ed.*, 2004, **43**, 2334; (*b*) G. Ferey, *Chem. Soc. Rev.*, 2008, **37**, 191; (*c*) H. C. Zhou, J. R. Long and O. M. Yaghi, *Chem. Rev.*, 2012, **112**, 673 and references cited therein; (*d*) H. C. Yang, K. Aoki, H. G. Hong, D. D. Sackett, M. F. Arendt, S. K. Yau,

C. M. Bell and T. E. Mallouk, *J. Am. Chem. Soc.*, 1993, **115**, 11855.

2 (*a*) R. Yerushalmi, A. Scherz and M. E. van der Boom, *J. Am. Chem. Soc.*, 2004, **126**, 2700; (*b*) S. Hermes, F. Schröder, R. Chelmowski, C. Wöll and R. A. Fischer, *J. Am. Chem. Soc.*, 2005, **127**, 13744; (*c*) E. Biemmi, C. Scherb and T. Bein, *J. Am. Chem. Soc.*, 2007, **129**, 8054; (*d*) R. Haruki, O. Sakata, T. Yamada, K. Kanaizuka, R. Makiura, Y. Akita, M. Yoshimoto and H. Kitagawa, *Trans. MRS-J*, 2008, **33**, 629; (*e*) D. Zacher, R. Schmid, C. Wöll and R. A. Fischer, *Angew. Chem., Int. Ed.*, 2010, **50**, 176; (*f*) K. Otsubo, T. Haraguchi, O. Sakata, A. Fujiwara and H. Kitagawa, *J. Am. Chem. Soc.*, 2012, **134**, 9605; (*g*) P. Falcaro, D. Buso, A. J. Hill and C. M. Doherty, *Adv. Mater.*, 2012, **24**, 3153; (*h*) B. Liu, M. Tu, D. Zacher and R. A. Fischer, *Adv. Funct. Mater.*, 2013, **23**, 3790; (*i*) Y. Sakata, S. Furukawa, M. Kondo, K. Hirai, N. Horike, Y. Takashima, H. Uehara, N. Louvain, M. Meilikhov, T. Tsuruoka, S. Isoda, W. Kosaka, O. Sakata and S. Kitagawa, *Science*, 2013, **339**, 193; (*j*) P. Falcaro, F. Lapierre, B. Marmiroli, M. Styles, Y. Zhu, M. Takahashi, A. J. Hill and C. Doherty, *J. Mater. Chem.*, 2013, **1**, 42.

3 (*a*) J. V. Barth, G. Costantini and K. Kern, *Nature*, 2005, **437**, 671; (*b*) J. Sakamoto, J. Van Heijst, O. Lukin and A. D. Schlüter, *Angew. Chem., Int. Ed.*, 2009, **48**, 1030; (*c*) U. Schlickum, R. Decker, F. Klappenberger, G. Zoppellaro, S. Klyatskaya, M. Ruben, I. Silanes, A. Arnau, K. Kern, H. Brune and J. V. Barth, *Nano Lett.*, 2007, **7**, 3813; (*d*) R. Madueno, M. T. Räisänen, C. Silien and M. Buck, *Nature*, 2008, **454**, 618; (*e*) Q. H. Wang and M. C. Hersam, *Nat. Chem.*, 2009, **1**, 206.

4 K. S. Novoselov, A. K. Geim, S. V. Morozov, D. Jiang, M. I. Katsnelson, I. V. Grigorieva, S. V. Dubonos and A. A. Firsov, *Nature*, 2005, **438**, 197.

5 (*a*) K. Akatsuka, M.-A. Haga, Y. Ebina, M. Osada, K. Fukuda and T. Sasaki, *ACS Nano*, 2009, **3**, 1097; (*b*) M. Osada, K. Akatsuka, Y. Ebina, H. Funakubo, K. Ono, K. Takada and T. Sasaki, *ACS Nano*, 2010, **4**, 5225.

6 S. Acharya, B. Das, U. Thupakula, K. Ariga, D. D. Sarma, J. Israelachvili and Y. Golan, *Nano Lett.*, 2013, **13**, 409.

7 P. Kissel, R. Erni, W. B. Schweizer, M. D. Rossell, B. T. King, T. Bauer, S. Götzinger, A. A. Schlüter and J. Sakamoto, *Nat. Chem.*, 2012, **4**, 287.

8 (*a*) T. Kato and J. M. J. Frechet, *J. Am. Chem. Soc.*, 1989, **111**, 8533; (*b*) B. Q. Ma and P. Coppens, *Chem. Commun.*, 2003, 2290.

9 (*a*) R. Makiura, S. Motoyama, Y. Umemura, H. Yamanaka, O. Sakata and H. Kitagawa, *Nat. Mater.*, 2010, **9**, 565; (*b*) R. Makiura and H. Kitagawa, *Eur. J. Inorg. Chem.*, 2010, **24**, 3715; (*c*) S. Motoyama, R. Makiura, O. Sakata and H. Kitagawa, *J. Am. Chem. Soc.*, 2011, **133**, 5640.

10 (*a*) R. Makiura, K. Tsuchiyama and O. Sakata, *CrystEngComm*, 2011, **13**, 5538; (*b*) R. Makiura and O. Konovalov, *Sci. Rep.*, 2013, **3**, 2506, DOI: 10.1038/srep02506.

11 A. Dong, J. Chen, P. M. Vora, J. M. Kikkawa and C. B. Murray, *Nature*, 2010, **466**, 474.

12 (*a*) T. N. Milic, N. Chi, D. G. Yablon, G. W. Flynn, J. D. Batteas and C. M. Drain, *Angew. Chem., Int. Ed.*, 2002, **41**, 2117; (*b*) C. M. Drain, F. Nifiatis, A. Vasenko and J. D. Batteas, *Angew. Chem., Int. Ed.*, 1998, **37**, 2344.

13 (*a*) B. Berge, O. Konovalov, J. Lajzerowicz, A. Renault, J. P. Rieu, M. Vallade, J. Als-Nielsen, G. Grübel and J. F. Legrand, *Phys. Rev. Lett.*, 1994, **73**, 1652; (*b*) P. Fontaine, M. Goldmann, P. Muller, M.-C. Fauré, O. Konovalov and M. P. Krafft, *J. Am. Chem. Soc.*, 2005, **127**, 512; (*c*) Y. Lifshitz, Y. Golan, O. Konovalov and A. Berman, *Langmuir*, 2009, **25**, 4469.

